Evidence for Steady Heating: Observations of an Active Region Core with *Hinode* and *TRACE*

Harry P. Warren[1], Amy R. Winebarger[2], David H. Brooks[1,3]

ABSTRACT

The timescale for energy release is an important parameter for constraining the coronal heating mechanism. Observations of "warm" coronal loops ($\sim 1\,\mathrm{MK}$) have indicated that the heating is impulsive and that coronal plasma is far from equilibrium. In contrast, observations at higher temperatures ($\sim 3\,\mathrm{MK}$) have generally been consistent with steady heating models. Previous observations, however, have not been able to exclude the possibility that the high temperature loops are actually composed of many small scale threads that are in various stages of heating and cooling and only appear to be in equilibrium. With new observations from the EUV Imaging Spectrometer (EIS) and X-ray Telescope (XRT) on *Hinode* we have the ability to investigate the properties of high temperature coronal plasma in extraordinary detail. We examine the emission in the core of an active region and find three independent lines of evidence for steady heating. We find that the emission observed in XRT is generally steady for hours, with a fluctuation level of approximately 15% in an individual pixel. Short-lived impulsive heating events are observed, but they appear to be unrelated to the steady emission that dominates the active region. Furthermore, we find no evidence for warm emission that is spatially correlated with the hot emission, as would be expected if the high temperature loops are the result of impulsive heating. Finally, we also find that intensities in the "moss," the footpoints of high temperature loops, are consistent with steady heating models provided that we account for the local expansion of the loop from the base of the transition region to the corona. In combination, these results provide strong evidence that the heating in the core of an active region is effectively steady, that is, the time between heating events is short relative to the relevant radiative and conductive cooling times.

Subject headings: Sun: corona

[1]Space Science Division, Naval Research Laboratory, Washington, DC 20375

[2]Department of Physics, Alabama A&M, 4900 Meridian Street, Normal, AL 35762

[3]College of Science, George Mason University, 4400 University Drive, Fairfax, VA 22030

1. Introduction

The coronal heating problem is one of the most fundamental open questions in solar physics. The formation of the high temperature solar atmosphere is clearly related to the magnetic fields generated in the solar interior, but how this magnetic energy is converted to the thermal energy of the corona remains unknown. One important constraint on the coronal heating mechanism is the time scale for energy release. If energy is deposited into magnetic flux tubes on timescales that are very short compared to a characteristic cooling time, then the corona will be filled with loops that are close to equilibrium and appear to be steady. Active region observations have generally suggested that high temperature loops are consistent with steady heating (e.g., Porter & Klimchuk 1995; Kano & Tsuneta 1995). These studies have found that the observed evolution of the emission is much slower than the radiative and conductive cooling timescales. There has also been some success in modeling entire active regions with steady heating models (Schrijver et al. 2004; Warren & Winebarger 2006; Winebarger et al. 2008; Lundquist et al. 2008). Finally, Antiochos et al. (2003) have argued that observations of the "moss," the footpoints of high temperature loops, are also consistent with steady heating. They found that the average moss intensities are typically constant over many hours and loops cooling through 1 MK were not observed in the moss region they observed.

There is considerable evidence that coronal loops observed at lower temperatures ($\sim$ 1 MK) are evolving and not in equilibrium (e.g., Aschwanden et al. 2001; Winebarger et al. 2003; Cirtain et al. 2007; Ugarte-Urra et al. 2009). These "warm" loops appear to have apex densities that are much higher than can be accounted for by steady heating models (e.g., Winebarger et al. 2003; Aschwanden et al. 2008). The properties of the warm loops are more consistent with impulsive heating models (e.g., Warren et al. 2002; Spadaro et al. 2003; Warren et al. 2003).

If it is true that hot loops are close to equilibrium while the warm loops are generally heated impulsively then the coronal heating mechanism becomes even more difficult to understand. The cooling time for short, hot loops is relatively rapid (typically a few hundred seconds), so heating events on these loops would need to occur very frequently. The cooling time for the warm loops is much longer (typically a few thousand seconds), so impulsive heating events on these loops would be infrequent.

It is tempting to conjecture that the emission at high temperatures is also consistent with impulsive heating models and that the apparent steadiness of this emission is the result of the superposition of many evolving stands along the line of sight (e.g. Cargill & Klimchuk 1997, 2004; Patsourakos & Klimchuk 2006). Previous observations have not been able to exclude this possibility. For example, it could be that the cooling loops are not easy to

detect in an active region core because they are faint relative to both the bright moss and the extended corona in which the active region is embedded.

The EUV Imaging Spectrometer (EIS) and the X-ray Telescope (XRT) on the *Hinode* mission provide a new opportunity to observe active region emission in unprecedented detail. EIS observes emission covering a very broad range of coronal temperatures: between Fe VII and Fe XXIV, only 4 ionization stages of Fe are not present in the EIS data (Fe XVIII–XXI). EIS also observes Ca XIV, XV, XVI, and XVII, providing excellent coverage of the critical temperature range around 3 MK (Warren et al. 2008). XRT is a broadband imaging telescope that observes high temperature plasma very efficiently and at high spatial resolution. The high cadence XRT data complement EIS, which often observes at a much lower cadence, and allows us to track the evolution of coronal plasma over a large field of view.

In this paper we use EIS and XRT observations to examine the properties of coronal plasma in the core of an active region. The active region that we have selected (NOAA active region 10960) is unusual in that most of the overlying warm loops are located to the north and south of the region, providing a largely unobstructed view of the active region core over a wide range of temperatures (see Figure 1). High cadence EIS observations of this region, which was observed by *Hinode* during the period 4–13 June 2007, have shown that the Fe XII 195.119 Å intensities, Doppler shifts, and non-thermal widths in the moss are constant over long periods of time, suggesting steady heating (Brooks & Warren 2009). In this study we find three additional lines of evidence that also indicate that the heating of high temperature loops is steady. We examine the evolution of the emission in individual pixels in XRT and find that the vast majority of the emission is constant to within approximately 15% during this period. The inspection of emission at different temperatures in the core of the active region shows that there is no evidence for loops cooling from high temperatures. We find no relationship between the warm emission (Fe X–Fe XIV) and the steady hot emission (Ca XIV–Ca XVII). Finally, we find that we can bring all of the observed moss intensities into agreement with steady heating models, if we allow for loop constriction at the base of the loop. Previous modeling work had found significant discrepancies at the lowest temperatures observed with EIS (Warren et al. 2008).

None of these observations is conclusive; they do not necessarily exclude alternative models that involve non-equilibrium processes. However, these observations do provide very strong constraints on the mechanism responsible for producing the high temperature emission observed in solar active regions.

2. Observations

The EIS instrument on *Hinode* is a high spatial and spectral resolution imaging spectrograph. EIS observes two wavelength ranges, 171–212 Å and 245–291 Å, with a spectral resolution of about 22 mÅ and a spatial resolution of about 1″ per pixel. There are 1″ and 2″ slits as well as 40″ and 266″ slots available. The slit-slot mechanism and the CCD both image an area on the Sun 1024″ in height, but a maximum of 512 pixels on the CCD can be read out at one time. Solar images can be made using one of the slots or by stepping one of the slits over a region of the Sun. Telemetry constraints generally limit the spatial and spectral coverage of an observation. See Culhane et al. (2007) and Korendyke et al. (2006) for more details on the EIS instrument.

For these observations the 1″ slit was stepped over the central part of the active region and 25 s exposures were taken at each position. An area of $128″ \times 128″$ was imaged in about 57 minutes (see Figure 1). The observing sequence for this observation returned the complete wavelength range from each detector so all of the lines observable with EIS are potentially available in these data.

The raw data were processed using `eis_prep` to remove dark current, warm pixels, and other instrumental effects using standard software. During the processing the observed count rates are converted to physical units. Intensities from the processed data are computed by fitting the observed line profiles with Gaussians. One line of particular interest that requires special attention is Ca XVII 192.858 Å, which is strongly blended with Fe XI 192.813 Å and an O V multiplet near 192.90 Å. An algorithm for deconvolving this blend using Fe XI 188.216 Å and multi-component fitting has been developed and is discussed in detail by Ko et al. (2009). We use this approach here to determine the Ca XVII intensities. The uncertainties for this line are significantly greater than for the other lines that we consider. However, as illustrated by the EIS rasters shown in Figure 2, there is a strong similarity between the deconvolved Ca XVII 192.858 Å image and other rasters from ions formed at similar temperatures, such as Ca XV 200.972 Å and Fe XVII 254.87 Å.

The XRT on *Hinode* is a high cadence, high spatial resolution (approximately 1″ pixels) grazing incidence telescope that images the Sun in the soft X-ray and extreme ultraviolet wavelength ranges. Temperature discrimination is achieved through the use of focal plane filters. Because XRT can observe the Sun at short wavelengths, XRT images can observe high temperature solar plasma very efficiently. The thinner XRT filters allow longer wavelength EUV emission to be imaged and extend the XRT response to lower temperatures. Further details on XRT are given in Golub et al. (2007).

The XRT data taken around the time of the EIS raster consisted of relatively high

cadence Open/Ti-Poly images with Open/Al-thick, Open/Be-thick, and G band images interleaved at a cadence of about 600 s. For this analysis we have processed all of the Open/Ti-Poly images with `xrt_prep` to remove the dark current and to do exposure time normalization. All of the images have been co-aligned to the initial frame using cross correlation. To investigate the longer term evolution of this region we have considered all of the XRT data within ± 2 hours of the start of the EIS raster. An example XRT image is given in Figure 1. An animation of these data is available in the electronic version of the manuscript.

In this analysis we also make reference to observations from *TRACE*, the *Transition Region and Coronal Explorer* (Handy et al. 1999). *TRACE* is a normal incidence, multi-layer telescope. There are 3 channels for imaging the corona: Fe IX/x 171 Å, Fe XII 195 Å, and Fe XV 284 Å. There is also a long wavelength channel for imaging the photosphere, chromosphere, and transition region. All of the images are projected onto a single CCD and images in different wavelengths must be taken sequentially. For these observations the data are mostly from the 171 Å channel, with a few white light, 1600 Å, and 284 Å images taken for context. The 171 Å data were processed with `trace_prep`, despiked, and co-aligned using cross-correlation. An example TRACE 171 Å image is given in Figure 1. An animation of the data is available in the electronic version of the manuscript.

3. Analysis

In this section we presented a detailed analysis of the EIS, XRT, and *TRACE* data available for this period. The EIS data represent a snapshot of the active region accumulated over about an hour and yield little insight into the temporal evolution of the emission. The XRT and TRACE observations, in contrast, have excellent temporal coverage but somewhat limited diagnostic capabilities. In combination they allow us to establish a detailed understanding of the plasma properties in the core of an active region and how they evolve in time.

3.1. Temporal Evolution

As is suggested by the four-hour XRT movie associated with Figure 1, the large scale pattern of the soft X-ray emission from this region is remarkably steady. To illustrate this we have selected several points from the core of the active region and plotted light curves for the emission in these individual pixels. The light curves, shown in Figure 3, generally show fluctuation levels of about 10–15% around the median intensity for this time interval.

In Figure 3 we also show two points that illustrate the evolution of transient loops. The lifetimes of these brightenings are generally on the order of $1000\,$s or less and show that the intensities in the core of the active region are steady on timescales that are long compared to a cooling time.

A more systematic view of the variability is obtained by computing the median intensity ($\bar{I}$) and standard deviation (σ_I) for each point in the co-aligned XRT data cube. A spatially resolved plot of $\sigma_I/\bar{I}$ is shown in Figure 4. Note we have considered only those pixels with median intensities above $50\,$DN s^{-1}. Low intensities well outside the core of the active region are highly variable.

This calculation shows that there a few structures in the core of the active region that are highly variable, such as those illustrated in Figure 3, but that the emission in most of the active region is constant to within approximately 15%. Shimizu (1995) performed a comprehensive study of active region transient brightenings with the Soft X-ray Telescope on *Yohkoh*. He found that the distribution of event energies followed a power-law distribution and that the total energy in these events was about a factor of 5 smaller than the energy required to heat the active corona. Our result is qualitatively consistent with this systematic study.

The XRT light curves suggest that the emission in the core of an active region is largely steady, with relatively few significant brightenings and a very high median intensity level ($> 1000\,$DN s^{-1}). This result is consistent with previous results from SXT (e.g., Porter & Klimchuk 1995; Kano & Tsuneta 1995), which showed that the observed emission decayed on timescales that were long relative to a cooling time. To put these observations in perspective, the cooling time for a $50\,$Mm loop cooling from equilibrium at $5\,$MK is of the order of $800\,$s, while the XRT emission is relatively steady for several hours. Note that a $50\,$Mm loop would connect the middle of the moss regions in this active region.

The core of the active region is clearly made up of the emission from many different loops and it is unclear if the low fluctuation levels are the result of steady heating on individual loops or from the superposition of many evolving loops (Cargill & Klimchuk 1997, 2004; Patsourakos & Klimchuk 2006). Models based on many evolving loops, however, predict that there should be warm emission ($\sim 1\,$MK) that is spatially correlated with the cooling of hot loops in the core of the active region (e.g., Warren & Winebarger 2007). Furthermore, the magnitude of the warm emission should be related to the observed intensity of the hot emission. Rising levels of hot emission should be accompanied by a similar increase in the warm emission. These predictions can be tested easily with the observations of this region with EIS.

3.2. Warm and Hot Emission

The interpretation of many active region observations is complicated by the presence of overlying warm loops. For this region such loops are largely, but not completely, absent, giving a relatively unobstructed view of the core of the active region at warm temperatures. This is illustrated by the TRACE 171 Å movies associated with Figure 1. In these movies we see large scale 1 MK loops to the north and south of the active region core but not over the core itself. We also do not see many loops cooling through the TRACE 171 Å bandpass that are connected to the moss, similar to the observations considered by Antiochos et al. (2003).

The limited amount of overlying emission allows us to look for any faint warm emission that is related to the formation of hot coronal loops. Another useful aspect of these observations is that there is a strong gradient in the intensities of the hot lines (Ca XIV–XVII, Fe XVII, and XRT) in the core of the active region in between the moss. To illustrate the behavior of the emission at different temperatures in the core of the active region we have selected a line segment parallel to the moss and extracted the intensities from each of the EIS rasters. These intensities are displayed in Figure 5 where we compare the intensities in each line with those from a hot line, Ca XV 200.972 Å. To facilitate the comparisons we have normalized the intensities to their values at the end of the line segment where the intensities of the hot lines are generally the smallest. For the hot lines the intensity along the segment increases by a factor of 3 to 4 in this region. At the cooler temperatures (Fe X–XIV), however, the intensities are unchanged and show no spatial correlation with the increase of the hot emission. The behavior of the emission from Fe XV and Fe XVI appears to fall in between the hot and warm lines, with Fe XVI following Ca XV fairly closely and Fe XV behaving more like a warm line.

Since the EIS raster lacks temporal information it is possible to argue that the more intense emission in the hot lines is evolving and will show up at a later time as enhanced emission at warmer temperatures. We have, however, already used the XRT observations to demonstrate that hot emission in the core is constant over many hours (Figure 3). Inspection of later XRT data for this active region shows that the strong gradients in the intensity and the dark inter-moss region actually persist for several days (see Brooks & Warren 2009 Figures 1 and 3). The hot emission shown in the EIS rasters is clearly not dominated by transient events.

We note that the intensities of the warm lines are non-zero in the core of the active region. Inspection of the TRACE image shown in Figure 1 suggests that while the inter-moss region is the dimmest part of the active region core, it is not the dimmest part of the active region at these temperatures. As we will show in the next section, almost all of the

warm lines have inter-moss intensities that are less than 20% of the moss intensities. The Fe XIII 202.044 Å line, however, is unusually bright in the inter-moss region. The lower level of the transition responsible for this line is very sensitive to collisonal de-excitation into other levels and the emissivity for this line rises sharply with decreasing density. This sensitivity to low density background plasma may account for the enhanced intensity of the Fe XIII 202.044 Å line in the inter-moss region.

The origin of the warm emission in the core of the active region is unclear. It is most likely related to unresolved, high lying loops that form around the active region (e.g. Mason et al. 1999). Scattered light from the bright moss may also influence the observed intensities in this region. See, for example, DeForest et al. (2009) for a discussion of scattered light in the *TRACE* instrument. Scattered light levels have not yet been measured in EIS, but because EIS and TRACE have several similar design elements, such as a front entrance filter supported by a mesh and multi-layer coatings, observations of dim regions with EIS are also likely to suffer from some level of stray light.

4. Modeling the Moss

The moss represents the footpoints of high temperature loops and offers important boundary conditions for physical models. Observations of the moss are particularly useful for constraining physical models since the observed intensity is proportional to the loop pressure and independent of the loop length (Martens et al. 2000; Vourlidas et al. 2001). That is,

$$I_\lambda \propto P_0 \times f \tag{1}$$

where I_λ is the observed intensity, P_0 is the base pressure, and f is the filling factor. This allows for the calculation of physical models of the moss without knowing the loop length. This is important since the magnetic topology of an active region is difficult to infer, even with the use of vector magnetograms (e.g., DeRosa et al. 2009).

Some previous work comparing EIS moss intensities with steady heating models has been presented in an earlier paper (Warren et al. 2008). This work introduced the use of density sensitive lines to determine both the base pressure and the filling factor. For lines formed close to Fe XII there was good agreement between steady heating models and the observations. At the lowest temperatures, however, there was a dramatic difference, with the modeled intensities being about 400% higher than what was observed. A similar temperature dependence in the contrast between moss and network intensities was noted by Fletcher & de Pontieu (1999). Their work suggested that it was difficult to identify moss regions in relatively low temperature emission.

Here we investigate the possibility that variations in the loop cross section are responsible for the relatively low moss intensities at low temperatures. For some time it has been recognized that magnetic flux tubes must expand rapidly in the region between the high beta photosphere and the low beta corona. That is, coronal loops must look like "funnels" in the transition region. This loop expansion plays an important role in determining the energy balance on coronal loops (e.g., Gabriel 1976; Dowdy et al. 1987; Rabin 1991) and needs to be accounted for in modeling the moss intensities. The network model of Gabriel (1976) shows a significant constriction at temperatures below about 1 MK, qualitatively similar to what has been suggested by the EIS observations of the moss.

The first step in performing detailed comparisons between theory and observation with these data is to accumulate the observed moss intensities from this active region. As shown in Figure 6, we follow Warren et al. (2008) and use a density sensitive line ratio to identify the dense moss regions. For this work we focus on the Fe XIII 203.826/202.044 Å ratio. The threshold has been set at $\log n_e = 9.7$ so that density contours encompass the bright region in the core of the active region. For each line we have extracted the intensities in this region and computed the distribution of intensities. The resulting distribution is approximately Gaussian and for each line we have determined the median intensity as well as the standard deviation in the distribution of intensities. A summary of all of the observed moss intensities is given in Table 1.

To account for any contamination from overlying loops or scattered light, we have subtracted an approximate background derived from the low intensity pixels in the inter-moss region. For consistency, the same background subtraction procedure is applied to all of the emission lines. The background intensities are given in Table 1.

It is unclear what uncertainties should be associated with these median intensities. The moss intensities are relatively high and the statistical errors in the fits to the Gaussian line profiles are generally small. Furthermore, for simplicity we will work with the median moss intensities and the uncertainties in these values are also small. Finally, the errors in our analysis are undoubtedly dominated by the systematic errors in the atomic data and by the assumptions embedded in the hydro modeling, such the assumption of ionization equilibrium. Absent any compelling alternative we assume that the uncertainty in each measured intensity is 15%, which is much higher than the statistical uncertainty.

Note that in a previous paper we used the Fe XII 186.880/195.119 line pair to identify the moss and determine the pressure and filling factor (Warren et al. 2008). Recent work, however, has shown that there are discrepancies between the various Fe XII and Fe XIII density sensitive line ratios (Young et al. 2009), leading one to wonder which densities are the most accurate. As we will discuss in more detail in the next section, the Si X 258.375/261.058 Å

ratio is generally consistent with the results from Fe XIII and we use the Fe XIII ratio here.

If we assume a constant loop cross section and steady, uniform heating, the only remaining parameters needed to solve the hydrodynamic loop equations are the volumetric heating rate and the loop length. As indicated by Equation 1, any family of solutions with the same base pressure will yield the same observed moss intensity. To illustrate this we calculate a grid of solutions that covers a range of loop lengths and heating rates. To solve the hydrostatic loop equations we use a numerical code written by Aad van Ballegooijen (e.g., Schrijver & van Ballegooijen 2005). We consider total loop lengths in the range $L = 10$–$100\,\mathrm{Mm}$ and heating rates that yield maximum temperatures in the range $\log T_{max} = 2.5$–$7.5\,\mathrm{MK}$. In the numerical model the lower boundary condition is set at $0.02\,\mathrm{MK}$ and the loops are assumed to be oriented perpendicular to the solar surface.

For each numerical solution we calculate the total intensity in the line using the usual expression

$$I_\lambda = \frac{1}{4\pi} \int \epsilon_\lambda(T_e, n_e) n_e^2 \, ds, \tag{2}$$

where $\epsilon_\lambda(T_e, n_e)$ is the emissivity computed from the CHIANTI atomic physics database version 5.2.1 (Dere et al. 1997; Landi et al. 2006). Figure 7 shows the calculated $203.826/202.044\,\text{Å}$ ratio as a function of the pressure at $1.5\,\mathrm{MK}$, the temperature of formation for Fe XIII. The ratio is clearly a function of the pressure alone and allows us to easily convert the observed line ratio into a value for the base pressure. An example calculation for the Fe XI $188.216\,\text{Å}$ intensity is also shown in Figure 7. With the pressure determined we can now read off the calculated intensities for each line. For Fe XI $188.216\,\text{Å}$, for example, the calculated intensity is $8625\,\mathrm{erg\,cm^{-2}\,s^{-1}\,sr^{-1}}$, which is much larger than what is observed and indicates that the emission is not resolved at the spatial resolution of EIS.

Calculated intensities for all of the emission lines are given in Table 1. We have estimated a filling factor of 20% using the median ratio of the observed to modeled intensities for the Fe X, XI, XII, and XIII lines. This corresponds to the Fe XI $188.216\,\text{Å}$ line. For the emission lines from these ions there is generally good agreement between the observed and modeled intensities. At lower temperatures, however, the observed intensities are much lower than what is calculated from the simulation. Ratios of the observed to modeled intensities as a function of temperature of formation are displayed in Figure 8. This plot shows that the constant area model breaks down at temperatures below about $1\,\mathrm{MK}$. This discrepancy is consistent with the comparisons presented previously (Warren et al. 2008).

An alternative approach to modeling the observed emission is to assume a loop length and determine the heating rate and filling factor that best fits the observed intensities. This method is based on the assumption that the observed moss intensities are independent of the

loop length, an assumption supported by theory (Martens et al. 2000) and by the numerical solutions presented here. This method has the advantage of being extensible. Our goal is to consider loops with complex geometries and the intensity-pressure approach outlined in the previous paragraphs becomes very cumbersome when applied to models with several free parameters. We have implemented such an approach using the Levenberg-Marquardt least-squares minimization routine MPFIT for the Interactive Data Language (IDL). The resulting modeled intensities are presented in Table 1 and are very similar to those derived from the intensity-pressure relationships. We have assumed a loop length of 50 Mm and obtain best-fit parameters of $\epsilon_0 = 5.98 \times 10^{-3}\,\mathrm{erg\ cm^{-3}\ s^{-1}}$ and $f = 0.22$. Only the emission lines formed at Fe X and above are considered in the minimization. In this approach all of the lines of interest are considered simultaneously and the pressure indicated by the Fe XIII lines is not necessarily reproduced by the model. To emphasize these lines in the final solution we reduce the uncertainties assumed for these lines to 5%.

To explore the role of geometry in determining the observed intensities we parametrize the cross-sectional area as a function of height using the following expression

$$A(s) = \frac{1}{\Gamma}\left\{1 + \frac{\Gamma - 1}{2}\left[\tanh\left(\frac{s - s_0}{\sigma_s}\right) + 1\right]\right\},\tag{3}$$

for $s < L/2$. The area is extended to the other footpoint by symmetry. The area expansion is defined so that the minimum is $A(s = 0) \approx 1/\Gamma$ and the maximum is $A(s = L/2) \approx 1$. The gradient in area expansion peaks at s_0 and the magnitude of the gradient is inversely proportional to σ_s. Smaller values of σ_s indicate a sharper transition. This form has been assumed because it allows for the loop expansion to be localized. Previous work has considered functions of the form $A \sim T^\alpha$, where the expansion continues throughout the corona (e.g., Rabin 1991; Chae et al. 1998). There is considerable empirical evidence that coronal loops have constant cross sections (e.g., Klimchuk 2000) and our area function is consistent with this. Note that in our prescription the loop geometry is fixed and does not respond to heating within the loop.

The expectation is that the constriction will reduce the calculated intensities at the low temperatures. The discrepancy between the observed intensities appears to occur around the temperature of formation of Fe X, which is approximately 1 MK. In the constant cross-section case this temperatures occurs at about 0.5 Mm up the loop length.

To solve for the best-fit parameters we assume a loop length of 50 Mm and use the Levenberg-Marquardt approach. The free parameters are the volumetric heating rate (ϵ_0), the filling factor (f), and the loop expansion parameters Γ, s_0, and σ_s. An example solution is shown in Figure 9 and the corresponding calculated intensities are given in Table 1. The solutions to the constant cross section and funnel models are generally similar. The

constant cross section model has somewhat higher temperatures and lower densities. The most significant impact on the calculated intensities comes from the area term in the emission measure

$$EM = A(s)n_e^2 \, ds. \tag{4}$$

The funnel model clearly reproduces the intensities at the lower temperatures much better than the constant cross-section models do. In this fit all of the emission lines are used. To emphasize the Fe XIII lines over the other lines the error assumed for the Fe XIII intensities is again reduced to 5%.

Previous studies on the transition region geometry (e.g., Rabin 1991; Chae et al. 1998) have considered the area as a function of temperature and for comparisons with these works we show $A(T(s))$ derived from the model parameters and the solution to the loop equations in Figure 10. Our result is qualitatively similar to the most promising funnel model derived by Rabin (1991, see model "B4HL" in their Figure 12). In this model the area is relatively constant until $\log T \approx 5.6$ and then expands rapidly, similar to what we show in Figure 9. Our result, however, is not consistent with the model derived by Chae et al. (1998) from SUMER Doppler shift measurements (see their Figure 19). Their model shows significant expansion at temperatures above $\log T \approx 5.0$. In both cases, as the authors were well aware, comparisons were made with spatially averaged quiet Sun observations and the applicability of these results to our modeling of the active region moss is unclear. Patsourakos et al. (1999) used spatially resolved measurements of the quiet network to examine loop expansion from the transition region to the corona. The amount of loop expansion that they measured is generally similar to what we have determined here, although it appears to begin at a somewhat lower temperature than in our model.

One factor that we have not considered is the impact of chromospheric absorption on the moss intensities. De Pontieu et al. (1999) have shown that the evolving, reticulated pattern of the moss is often related to obscuration by chromospheric jets on neighboring field lines. Absorption leads to reduced observed intensities and impacts the filling factors and heating rates determined from the observations. This chromospheric absorption could also be stronger at the lowest heights and could explain the lower intensities of the lower temperature lines. This could also potentially complicate the inference of the transition region geometry from the observed intensities. Recent analysis of coordinated EIS and SUMER observations suggests that emission below the Lyman continuum is reduced by about a factor of 2 (De Pontieu et al. 2009). It should be noted that this result is predicated on comparisons between 2 Fe XII line ratios (186.880/195.119 Å and 1241.990/195.119 Å). As we have discussed, the atomic data for Fe XII is problematic and there is some uncertainty in this correction. The results from Fe XII also do not yield insights into the possibility of additional absorption at lower heights. Clearly more analysis is needed on this important

issue.

5. Electron Densities

In this paper we have used the Fe XIII 203.826/202.044 Å line ratio to determine the electron density while previously the Fe XII 186.880/195.119 Å ratio was used. The Fe XII ratio is sensitive over a very wide range of densities ($\log n_e = 7 - 12$), making it a very useful plasma diagnostic. It has been found, however, that the Fe XIII and Fe XII densities generally don't agree (Young et al. 2009), leading to the potential for systematic errors in the modeling.

In many previous studies the atomic data for Si has proven to be very robust (e.g, Feldman et al. 1999; Doschek et al. 1997) and so we have compared the densities derived from the Si X 258.375/261.058 Å ratio with those from the other line pairs. The Si X ratio is sensitive over a much smaller range of densities than the Fe XII and Fe XIII pairs so we have looked for observations of all three line pairs in small active regions, bright points, and the quiet Sun, i.e., regions where the densities are generally lower than in the moss region that we have studied here.

The result of one such comparison is shown in Figure 11. This plot shows the densities computed in a small active region from all three line pairs. These calculations clearly show that at high densities the Fe XII results are systematically higher than those from Fe XIII and Si X and that the Fe XIII and Si X densities are in good agreement. We have found similar results from the analysis of 4 other quiet Sun and active region observations.

The problems with Fe XII become more pronounced at the highest densities, which is particularly problematic for the analysis of the moss. In these observations the peak density is about a factor of 3 higher in Fe XII. Since the observed intensity scales with the square of the density this discrepancy is amplified. We have derived filling factors of 10–20% for this moss region. Emphasizing the Fe XII ratio would lead to filling factors almost an order of magnitude smaller.

6. Summary

We have presented a comprehensive analysis of observations in the core of an active region using data from the EIS and XRT instruments on *Hinode* and *TRACE*. The apparent steadiness of the XRT emission, the lack of spatial correlation between the hot and warm emission, and the consistency of the funnel models with the observed emission all point to

frequent heating events that keep the hot loops close to equilibrium. Furthermore, these results are consistent with high cadence EIS measurements of moss intensities, Doppler shifts, and nonthermal widths that show little evidence of dynamical events over many hours (Brooks & Warren 2009). In combination, these results provide strong evidence that the heating in the core of an active region is effectively steady, that is, the time between heating events is short relative to the relevant radiative and conductive cooling times.

REFERENCES

Antiochos, S. K., Karpen, J. T., DeLuca, E. E., Golub, L., & Hamilton, P. 2003, ApJ, 590, 547

Aschwanden, M. J., Nitta, N. V., Wuelser, J.-P., & Lemen, J. R. 2008, ApJ, 680, 1477

Aschwanden, M. J., Schrijver, C. J., & Alexander, D. 2001, ApJ, 550, 1036

Brooks, D. H., & Warren, H. P. 2009, ApJ, 703, L10

Cargill, P. J., & Klimchuk, J. A. 1997, ApJ, 478, 799

Cargill, P. J., & Klimchuk, J. A. 2004, ApJ, 605, 911

Chae, J., Yun, H. S., & Poland, A. I. 1998, ApJS, 114, 151

Cirtain, J. W., Del Zanna, G., DeLuca, E. E., Mason, H. E., Martens, P. C. H., & Schmelz, J. T. 2007, ApJ, 655, 598

Culhane, J. L., et al. 2007, Sol. Phys., 60

De Pontieu, B., Berger, T. E., Schrijver, C. J., & Title, A. M. 1999, Sol. Phys., 190, 419

De Pontieu, B., Hansteen, V. H., McIntosh, S. W., & Patsourakos, S. 2009, ApJ, 702, 1016

DeForest, C. E., Martens, P. C. H., & Wills-Davey, M. J. 2009, ApJ, 690, 1264

Dere, K. P., Landi, E., Mason, H. E., Monsignori Fossi, B. C., & Young, P. R. 1997, A&AS, 125, 149

DeRosa, M. L., et al. 2009, ApJ, 696, 1780

Doschek, G. A., Warren, H. P., Laming, J. M., Wilhelm, K., Lemaire, P., Schühle, U., & Moran, T. G. 1997, ApJ, 482, L109

Dowdy, J. F., Jr., Moore, R. L., & Emslie, A. G. 1987, Sol. Phys., 112, 255

Feldman, U., Doschek, G. A., Schühle, U., & Wilhelm, K. 1999, ApJ, 518, 500

Fletcher, L., & de Pontieu, B. 1999, ApJ, 520, L135

Gabriel, A. H. 1976, Royal Society of London Philosophical Transactions Series A, 281, 339

Golub, L., et al. 2007, Sol. Phys., 243, 63

Handy, B. N., et al. 1999, Sol. Phys., 187, 229

Kano, R., & Tsuneta, S. 1995, ApJ, 454, 934

Klimchuk, J. A. 2000, Sol. Phys., 193, 53

Ko, Y.-K., Doschek, G. A., Warren, H. P., & Young, P. R. 2009, ApJ, 697, 1956

Korendyke, C. M., et al. 2006, Appl. Opt., 45, 8674

Landi, E., Del Zanna, G., Young, P. R., Dere, K. P., Mason, H. E., & Landini, M. 2006, ApJS, 162, 261

Lundquist, L. L., Fisher, G. H., & McTiernan, J. M. 2008, ApJS, 179, 509

Martens, P. C. H., Kankelborg, C. C., & Berger, T. E. 2000, ApJ, 537, 471

Mason, H. E., Landi, E., Pike, C. D., & Young, P. R. 1999, Sol. Phys., 189, 129

Patsourakos, S., & Klimchuk, J. A. 2006, ApJ, 647, 1452

Patsourakos, S., Vial, J. C., Gabriel, A. H., & Bellamine, N. 1999, ApJ, 522, 540

Porter, L. J., & Klimchuk, J. A. 1995, ApJ, 454, 499

Rabin, D. 1991, ApJ, 383, 407

Schrijver, C. J., Sandman, A. W., Aschwanden, M. J., & DeRosa, M. L. 2004, ApJ, 615, 512

Schrijver, C. J., & van Ballegooijen, A. A. 2005, ApJ, 630, 552

Shimizu, T. 1995, PASJ, 47, 251

Spadaro, D., Lanza, A. F., Lanzafame, A. C., Karpen, J. T., Antiochos, S. K., Klimchuk, J. A., & MacNeice, P. J. 2003, ApJ, 582, 486

Ugarte-Urra, I., Warren, H. P., & Brooks, D. H. 2009, ApJ, 695, 642

Vourlidas, A., Klimchuk, J. A., Korendyke, C. M., Tarbell, T. D., & Handy, B. N. 2001, ApJ, 563, 374

Warren, H. P., Feldman, U., & Brown, C. M. 2008, ApJ, 685, 1277

Warren, H. P., & Winebarger, A. R. 2006, ApJ, 645, 711

Warren, H. P., & Winebarger, A. R. 2007, ApJ, 666, 1245

Warren, H. P., Winebarger, A. R., & Hamilton, P. S. 2002, ApJ, 579, L41

Warren, H. P., Winebarger, A. R., & Mariska, J. T. 2003, ApJ, 593, 1174

Warren, H. P., Winebarger, A. R., Mariska, J. T., Doschek, G. A., & Hara, H. 2008, ApJ, 677, 1395

Winebarger, A. R., Warren, H. P., & Falconer, D. A. 2008, ApJ, 676, 672

Winebarger, A. R., Warren, H. P., & Mariska, J. T. 2003, ApJ, 587, 439

Winebarger, A. R., Warren, H. P., & Seaton, D. B. 2003, ApJ, 593, 1164

Young, P. R., Watanabe, T., Hara, H., & Mariska, J. T. 2009, A&A, 495, 587

MDI 05–Jun–07 08:03:01

TRACE 171 07:44:58
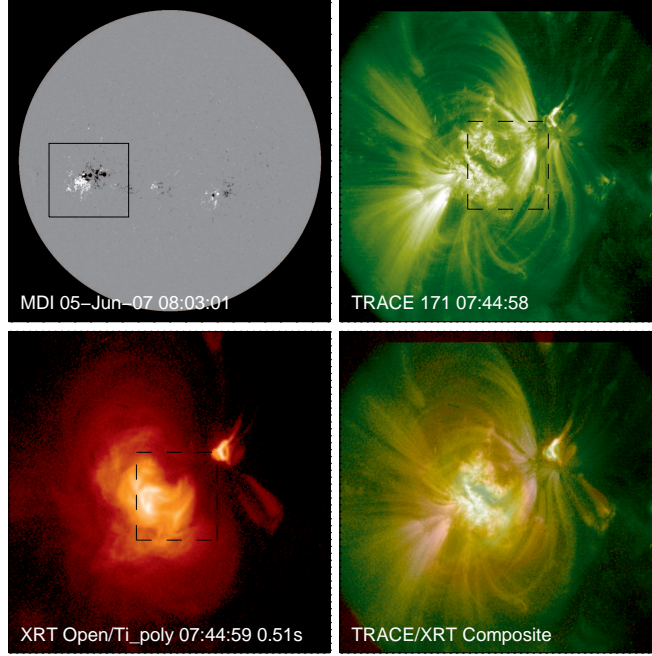
XRT Open/Ti_poly 07:44:59 0.51s

TRACE/XRT Composite

Fig. 1.— Context images for observations of NOAA active region 10960 taken on 5 June 2007. Top left panel: An MDI/*SoHO* magnetogram with the TRACE and XRT fields of view indicated. Top right and bottom left panels: TRACE 171 Å and XRT Ti-Poly images with the EIS field of view indicated. Bottom right panel: A composite TRACE and XRT image showing the difference in morphology between the hot and warm emission. Animations of the TRACE and XRT data are available with the electronic version of the manuscript (movie1_trace.mpg, movie1_trace_moss.mpg and movie2_xrt.mpg).

Fig. 2.— EIS rasters from the core of NOAA active region 10960 taken on 5 Jun 2007 between 06:48:20 and 07:44:59 UT. With the exception of Ca XVII 192.858 Å, which was deconvolved from a blend with other lines using a procedure described in the text, the intensities were derived from simple single or double Gaussian fits to the line profile.
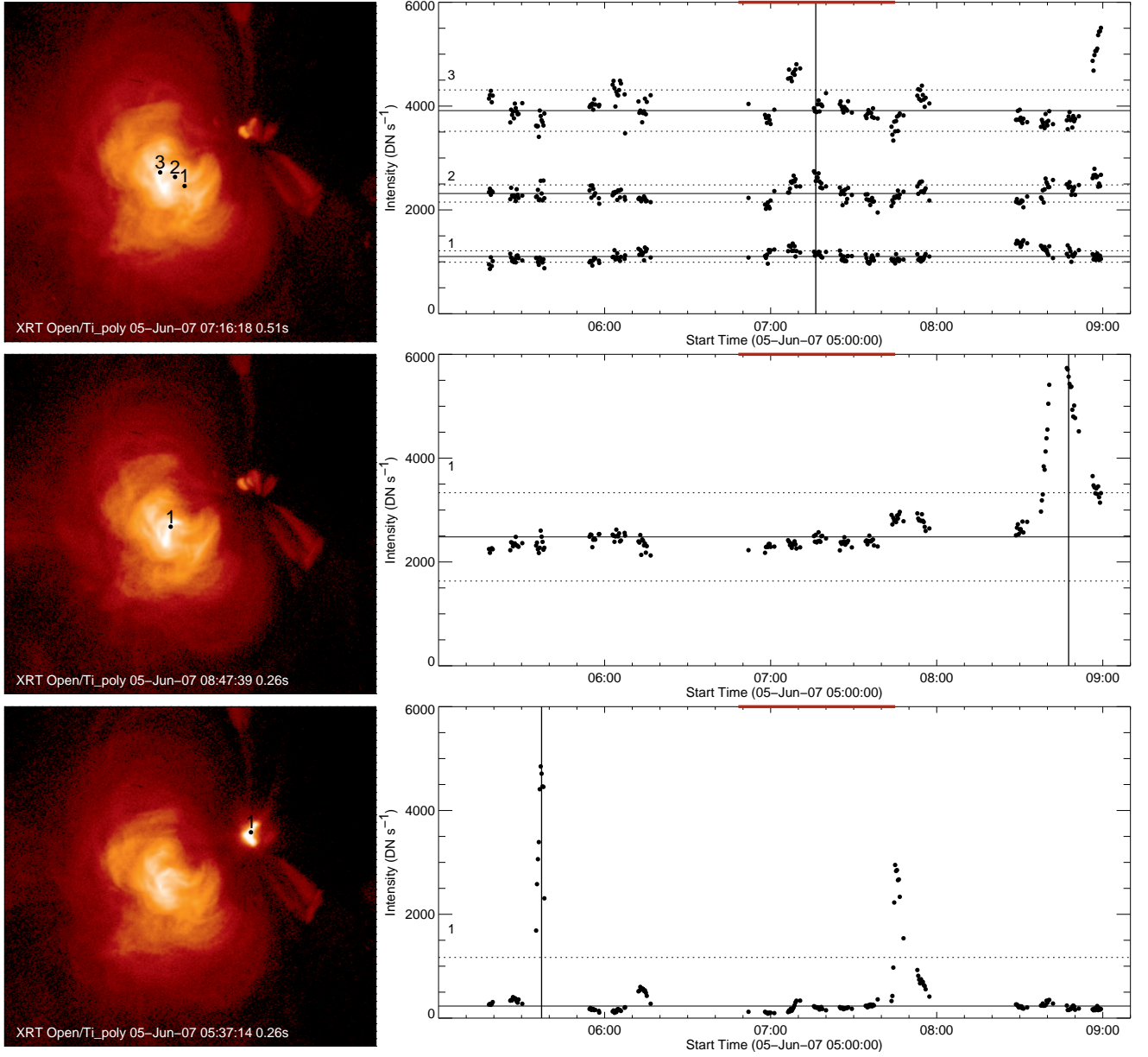
Fig. 3.— The evolution of the high temperature emission measured at various points in the active region core. The left panels show a single image from the XRT data set with the points indicated. The right panels show the light curves for these points. For each point the median intensity ($\bar{I}$) is indicated with a solid line and $\bar{I} \pm \sigma_I$ is indicated by the dashed lines. The red bar at the top of panel highlights the time of the EIS raster. The vertical line indicates the time of the XRT image displayed on the left. The top panel illustrates relatively constant emission that dominates the core of the active region. The bottom panels illustrate the evolution of more variable emission.
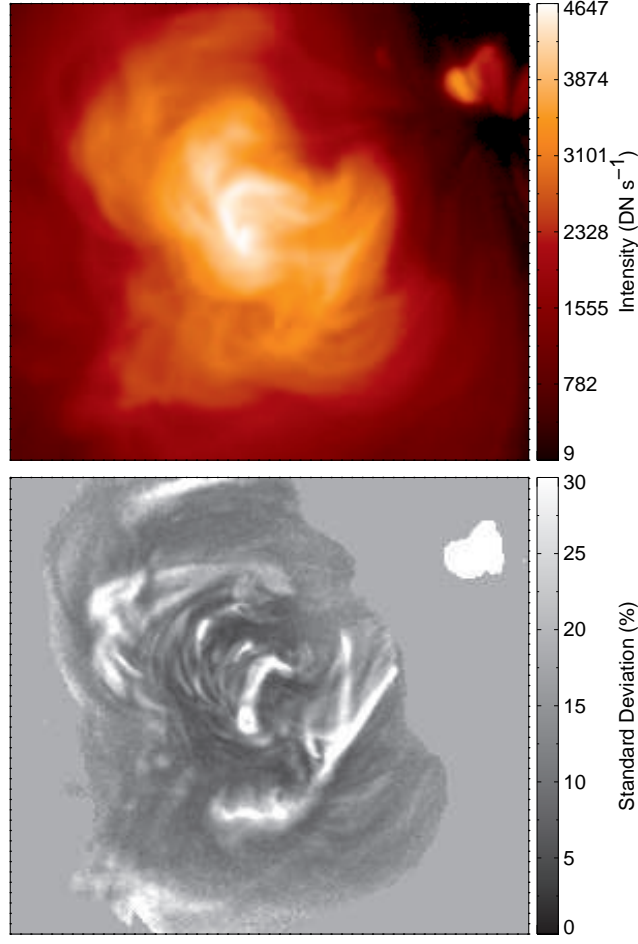
Fig. 4.— Plots of $\bar{I}$ and $\sigma_I/\bar{I}$ as a function of position for the XRT Open/Ti-Poly data. For the $\sigma_I/\bar{I}$ plot only the points with a median intensity above $50\,\mathrm{DN}\,\mathrm{s}^{-1}$ are shown. For low intensity pixels the fluctuation level is generally very high ($>30\%$).
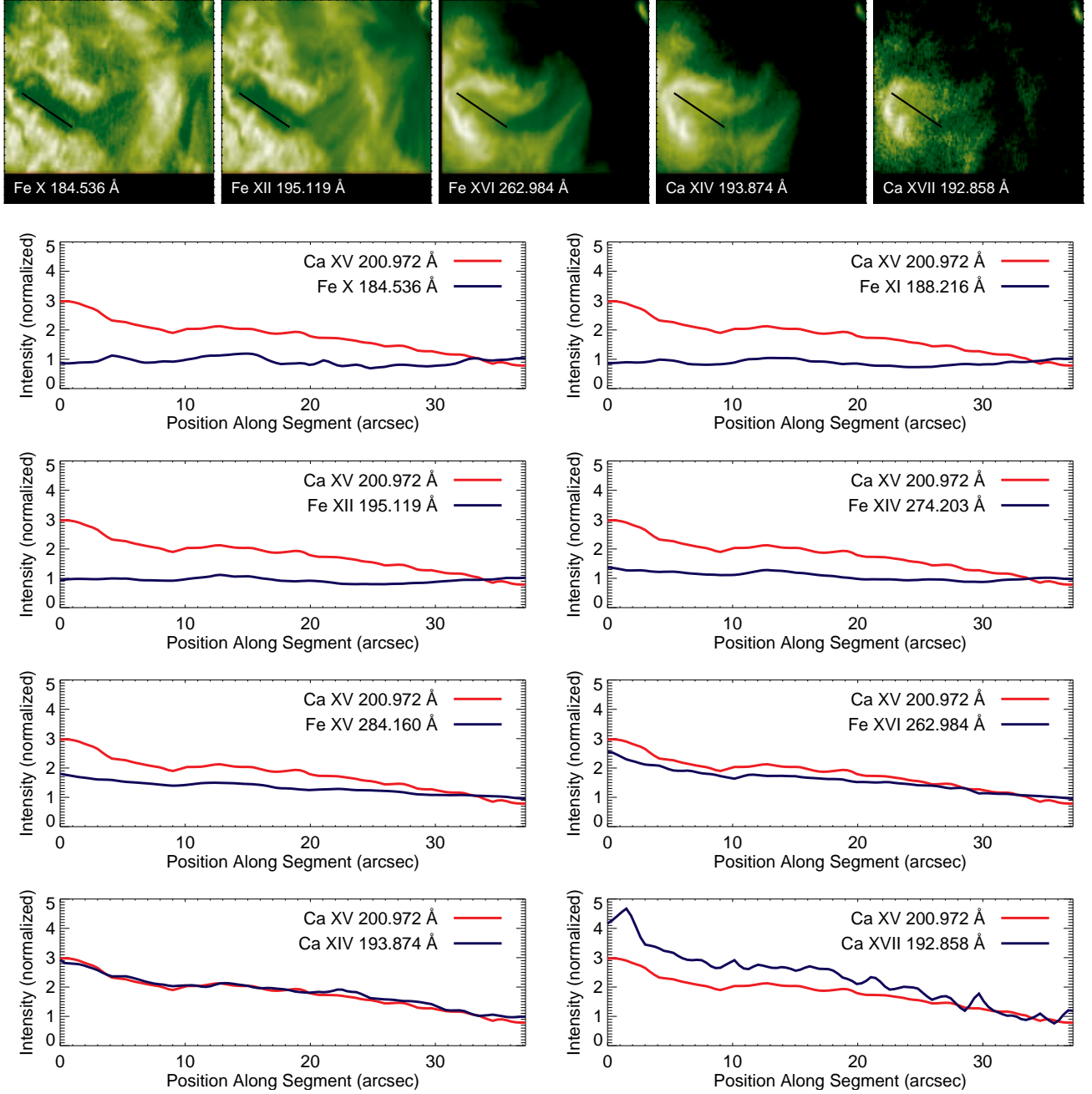
Fig. 5.— Intensities in the core of an active region. Top panels: EIS rasters in Fe X, Fe XII, Fe XVI, Ca XIV, and Ca XVII. Bottom panels: The intensities along a segment in various emission lines. For each plot the intensities are compared with Ca XV 200.972 Å. At the lowest temperatures (Fe X–Fe XV) there is little or no relationship between the hot and warm emission. At the highest temperatures (Fe XVI–Ca XVII) the intensities are strongly correlated. The intensities are normalized to the values at the end of the segment ($\sim 40''$).
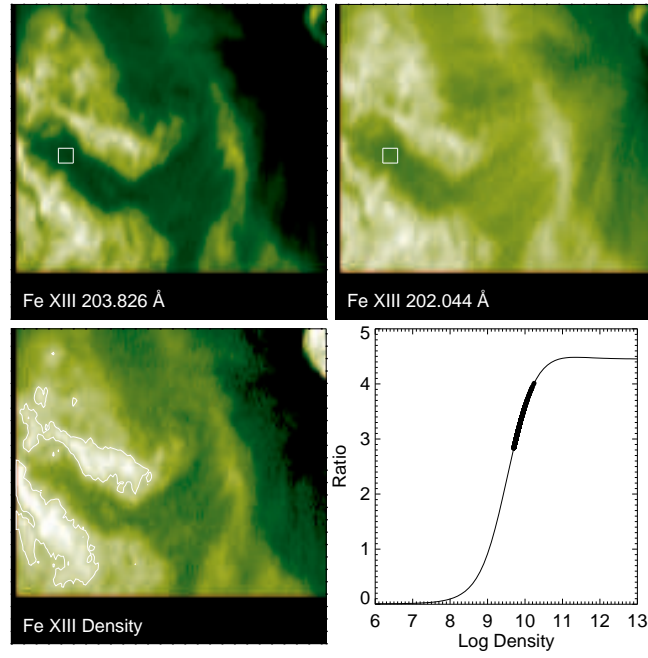
Fig. 6.— The moss identified using a simple threshold with the density derived from the Fe XIII 203.826/202.044 Å ratio. The contour is for $\log n_e = 9.7$. The box indicates the region used to estimate the background contribution to the line intensities. For each emission line considered here we have computed the median intensity in the moss and background regions.
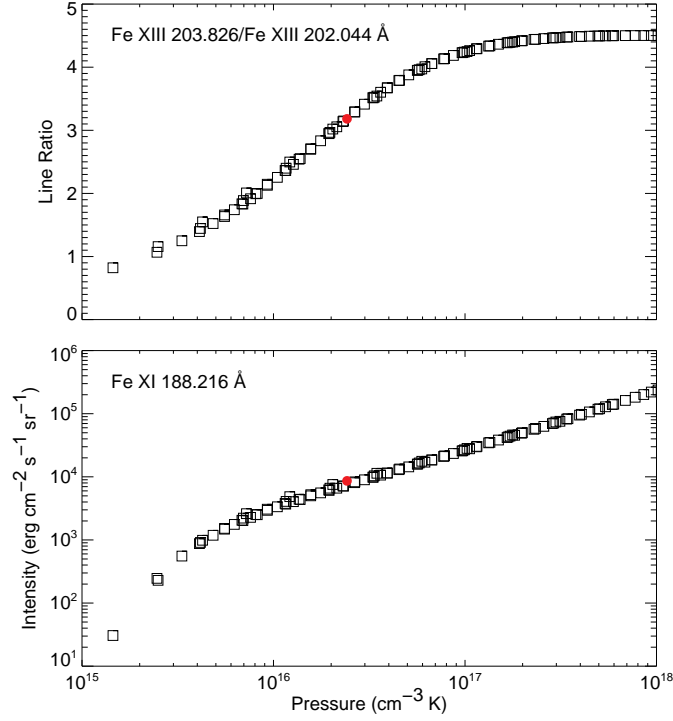
Fig. 7.— Top panel: The Fe XIII 203.826/202.044 Å ratio as a function of the pressure at 1.5 MK calculated from a steady heating model. Solutions over a range of loop lengths and volumetric heating rates have been used. The red dot represents the pressure corresponding to the median intensities given in Table 1. Bottom Panel: The intensity in the Fe XI 188.216 Å line as a function of pressure.
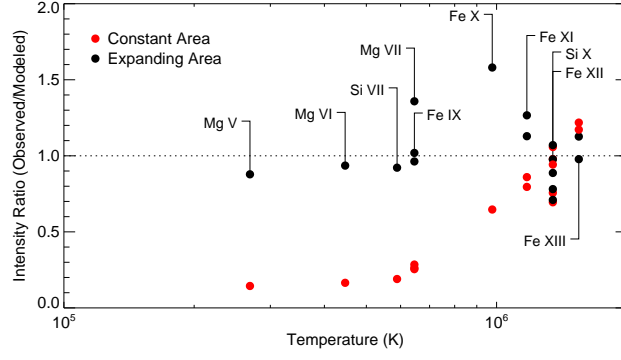
Fig. 8.— The ratio of observed to calculated intensity for the expanding area (or funnel) model and constant area models (const2) plotted as a function of temperature. This plot illustrates the failure of the constant cross-section models at low temperatures.
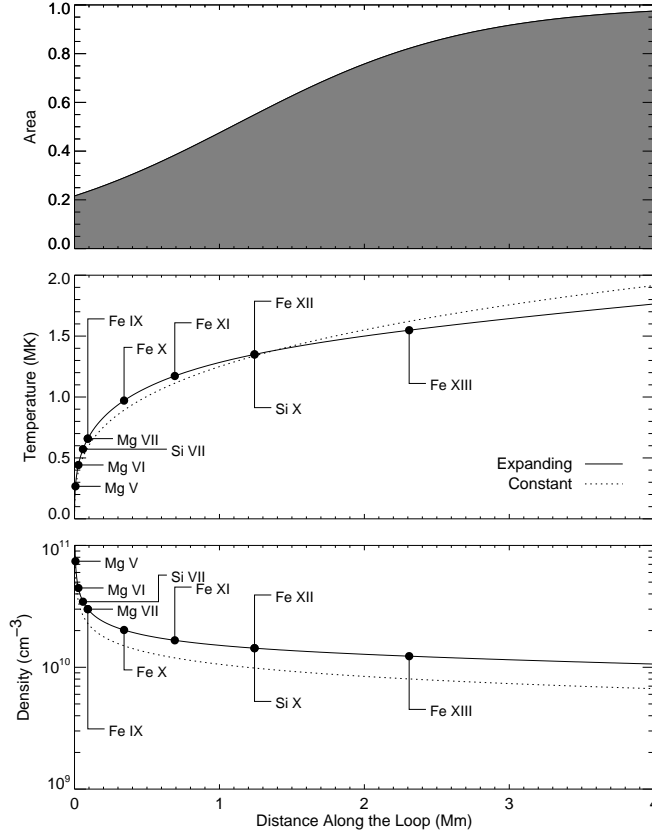
Fig. 9.— The transition region loop geometry derived from EIS observations of the Moss. Top panel: The normalized area as a function of distance along the loop. The best-fit parameters are $\epsilon_0 = 8.03 \times 10^{-3}$, $f = 0.11$, $\Gamma = 45.6$, $s_0 = 1.1\,\text{Mm}$, and $\sigma_s = 1.6\,\text{Mm}$. Bottom panels: The temperature and density along the loop. The peak temperature of formation for each ion is indicated on the plots. For comparison, the corresponding best-fit solution for the constant cross section case is also plotted. The total loop length is $50\,\text{Mm}$ and only part of the solution is shown.
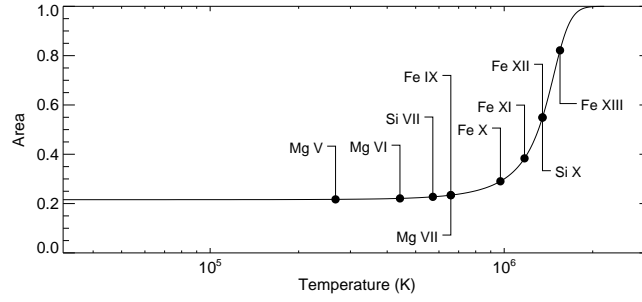
Fig. 10.— The area as a function of temperature for the expanding loop model shown in Figure 9. The peak temperature of formation for each ion is indicated.
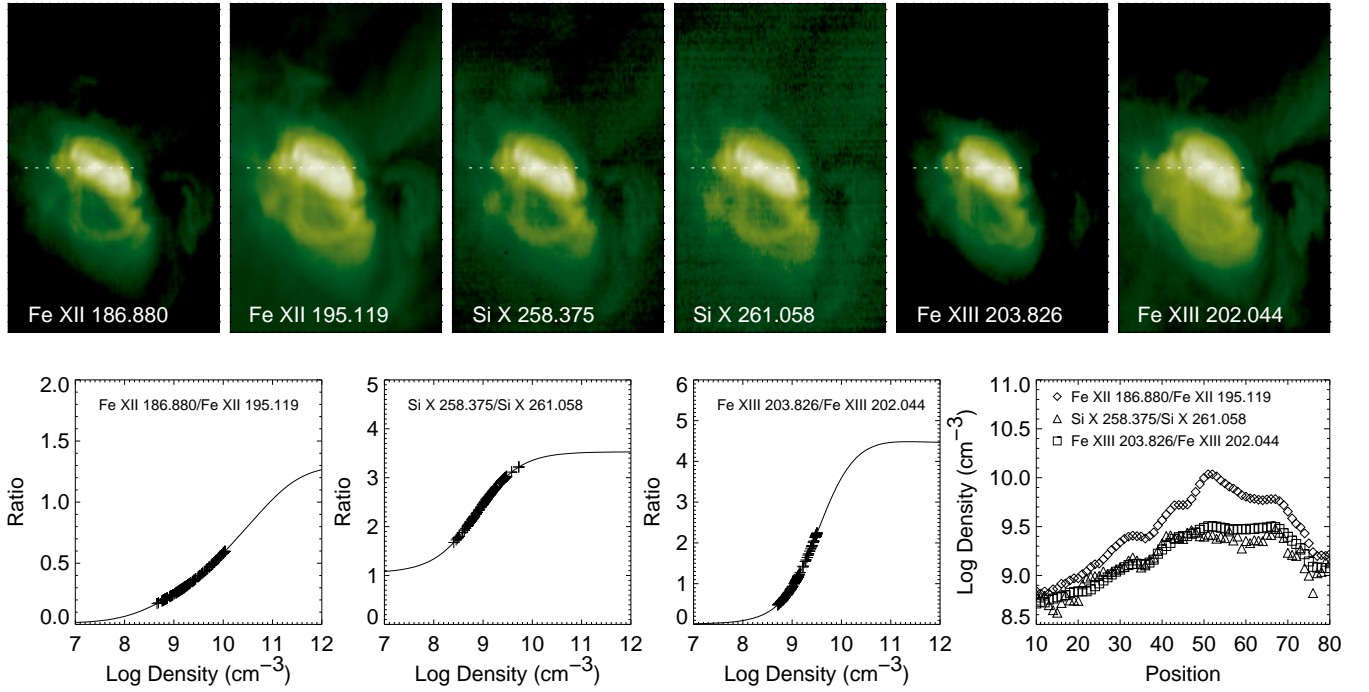
Fig. 11.— EIS observations of a small active region beginning on 2 December 2007 at 11:10:44 UT. Top panels: Rasters in 3 pairs of density sensitive lines. Intensities have been extracted from the region indicated by the white line. Bottom panels: Densities computed from the 3 pairs of lines. The final panel shows the densities as a function of position. The Fe XIII and Si X densities are in generally good agreement while the Fe XII densities are systematically higher.

Table 1.   Observed and Modeled Moss Intensities[a]

Ion	I_{median}	σ_I	I_{back}	$I_{observed}$	I_{const1}	R	I_{const2}	R	I_{funnel}	R
Mg V 276.579	36.4	12.4	3.1	33.3	178.3	0.19	231.3	0.14	38.0	0.88
Mg VI 270.394	97.8	25.9	8.5	89.3	420.1	0.21	541.3	0.16	95.4	0.94
Mg VII 280.737	96.7	27.5	5.1	91.6	247.1	0.37	321.4	0.28	67.4	1.36
Si VII 275.352	136.6	42.0	9.6	126.9	529.6	0.24	668.2	0.19	137.7	0.92
Fe IX 188.497	248.0	64.6	13.8	234.2	710.1	0.33	892.6	0.26	229.9	1.02
Fe IX 197.862	106.1	26.1	8.0	98.0	310.3	0.32	384.8	0.25	101.8	0.96
Fe X 184.536	936.9	225.3	62.3	874.6	1107.0	0.79	1352.1	0.65	553.3	1.58
Fe XI 182.167	1114.6	266.3	59.0	1055.6	1114.1	0.95	1326.6	0.80	935.0	1.13
Fe XI 188.216	1827.7	398.5	121.4	1706.4	1706.4	1.00	1984.4	0.86	1347.6	1.27
Si X 258.375	1390.2	301.4	65.4	1324.8	1171.6	1.13	1354.4	0.98	1355.8	0.98
Si X 261.058	455.0	97.3	24.7	430.3	355.0	1.21	406.9	1.06	402.0	1.07
Fe XII 186.880	3026.4	676.5	130.8	2895.6	2608.4	1.11	3072.6	0.94	3263.0	0.89
Fe XII 192.394	1309.5	266.7	81.9	1227.5	1443.1	0.85	1622.4	0.76	1571.6	0.78
Fe XII 195.119	4102.9	827.4	271.6	3831.3	4883.6	0.78	5516.1	0.69	5395.9	0.71
Fe XIII 202.044	2196.5	349.7	214.8	1981.7	1457.3	1.36	1626.5	1.22	1759.2	1.13
Fe XIII 203.826	6609.6	1284.1	304.9	6304.7	4633.7	1.36	5379.5	1.17	6446.1	0.98

[a]In this table wavelengths are in Å and the intensities are in erg cm^{-2} s^{-1} sr^{-1}. Note that σ_I is the Gaussian width for the distribution of intensities in the moss and not the statistical uncertainty. I_{back} is an estimate of the background emission in the moss. I_{const1} is the computed intensity for the constant cross-section model computed from the intensity-pressure relationships, I_{const2} is the constant cross-section model computed from the least-squares fitting, and I_{funnel} is the best-fit model for the funnel geometry. R is the ratio of observed to calculated intensities.